Spin-orbit relaxation and quenching of cesium $7\,^2P$ in mixtures of helium, methane, and ethane

Kirk C. Brown[*] and Glen P. Perram[†]

Department of Engineering Physics, Air Force Institute of Technology, WPAFB, Ohio 45433, USA
(Received 1 November 2011; published 23 February 2012)

The fine-structure mixing and quenching cross sections of the cesium $7\,^2P$ state in mixtures of helium, methane, and ethane were measured using laser-induced fluorescence techniques. This research was performed to study the kinetics associated with an optically pumped blue cesium laser operating on the $7\,^2P_{1/2}$-$6S_{1/2}$ transition. Fluorescence decay curves from pulsed-laser experiments were analyzed as a function of buffer gas density at cell temperatures near 393 K. The fine-structure mixing cross sections for He, CH_4, and C_2H_6 are 14 ± 3, 35 ± 6, and 73 ± 10 Å², respectively. The $^2P_{3/2}$ state is quenched more rapidly than the $^2P_{1/2}$ state. A model that includes the effects of radiation trapping and independent quenching cross sections for each fine-structure sublevel is compared to the experimental data. The rapid quenching negatively impacts the performance of a recently demonstrated optically pumped blue laser. We compare the cross sections for alkali-metal and noble gases and extend the adiabaticity analysis to the higher-lying excited states.

PACS number(s): 34.50.−s, 42.55.Lt, 42.62.Fi, 82.20.Pm

I. INTRODUCTION

Optically pumped alkali-metal lasers have been intensely studied during the past decade [1–6]. When pumped with a diode array, slope efficiency can exceed 80% [2]. These systems appear promising for scaling to high average power. For example, a rubidium laser pumped by a 1.28-kW diode stack with a 0.35-nm bandwidth has recently achieved 145 W average power [4]. The energy level diagram of some lower energy levels of the cesium system is illustrated in Fig. 1, and the wavelengths and transition probabilities are listed in Table I. The near-infrared laser is diode pumped from the ground $6\,^2S_{1/2}$ state to the first excited $6\,^2P_{3/2}$ state at 852 nm and lases after spin-orbit relaxation from $6\,^2P_{1/2}$ at 894 nm. The fine-structure splitting of the $6\,^2P$ term is 554 cm^{-1} and relaxation by molecular collision partners such as ethane or methane at several hundred Torr is required.

Several optically pumped alkali-metal lasers operating in the blue from the second excited $7\,^2P_{3/2,1/2}$ states have also been demonstrated. Two-color sequential excitation [7] and two-photon direct excitation of the $6\,^2D_{3/2,1/2}$ states [5] followed by optical cascade to the $7\,^2P$ states, or direct one-photon excitation of the $7\,^2P$ states [8] have been investigated. However, the fine-structure relaxation and collisional quenching of these states are relatively unstudied. For Cs $7\,^2P_{3/2,1/2}$, there are several older reports of rapid fine-structure mixing by rare gases [9–11] and molecular collision partners [12], but not for the important laser species, ethane. The corresponding quenching rates, their dependence on spin-orbit split state, and the product states are largely unavailable. Inter-multiplet energy transfer between $7\,^2P_{3/2,1/2}$ and $6\,^2D_{3/2}$ states with rare gas partners are relatively slow, with the exception being He [10]. The presence of additional electronic levels, which are not a factor for the first ^2P state, induces a barrier structure in the potential that reduces the cross section. For the case of He, that barrier structure is absent allowing the collision to proceed via long-range forces, increasing the cross section.

The rates for fine-structure mixing of the lowest ^2P states in the alkali metals for collisions with rare gases increase with decreased splitting, as predicted by adiabaticity arguments [13, 14]. When the splitting is large and the collision energy is low, the duration of the collision is long relative to the oscillation period and the rates are slow. The more impulsive collision for the helium-potassium system leads to faster rates. Similar effects have been observed for the higher-lying excited alkali-metal states where the fine-structure splitting is less. For example, collision cross sections with noble gases and the $7\,^2P$ states are larger by a factor of 10^2–10^3 than those of the $6\,^2P$ state [9,15]. For the $8\,^2P$ state the values are larger by another factor of 10, corresponding to a reduction in the fine-structure splitting [10].

In the present work, pulsed-laser-induced fluorescence techniques are employed to measure the fine-structure mixing and J-dependent quenching rates for the Cs $7\,^2P_{3/2,1/2}$ states.

II. THEORY

A. Derivation of eigenvalues

In this section we derive the key relationships for determining the spin-orbit mixing and quenching cross sections. The populations in the ground state $6\,^2S_{1/2}$, N_0, and the second excited states $7\,^2P_{3/2}$, N_2, and $7\,^2P_{1/2}$, N_1, are controlled by the following mechanism:

$$[\text{Cs}(6S_{1/2})] + h\nu_{20} \xrightarrow{R} [\text{Cs}(7P_{3/2})], \quad \text{optical pumping}, \tag{1a}$$

$$[\text{Cs}(7P_{3/2})] \xrightarrow{\xi_2 A_{20}} [\text{Cs}(6S_{1/2})] + h\nu_{20}, \quad \text{spontaneous emission}, \tag{1b}$$

$$[\text{Cs}(7P_{1/2})] \xrightarrow{\xi_1 A_{10}} [\text{Cs}(6S_{1/2})] + h\nu_{10}, \quad \text{spontaneous emission}, \tag{1c}$$

$$[\text{Cs}(7P_{3/2})] + M \xrightarrow{k_{20}} [\text{Cs}(S,P,D)] + M, \quad \text{quenching}, \tag{1d}$$

$$[\text{Cs}(7P_{1/2})] + M \xrightarrow{k_{10}} [\text{Cs}(S,P,D)] + M, \quad \text{quenching}, \tag{1e}$$

$$[\text{Cs}(7P_{3/2})] + M \underset{k_{12}}{\overset{k_{21}}{\rightleftarrows}} [\text{Cs}(7P_{1/2})] + M, \quad \text{spin-orbit mixing}, \tag{1f}$$

---

[*]Current address: Defense Threat Reduction Agency, Ft. Belvoir, VA 22060.

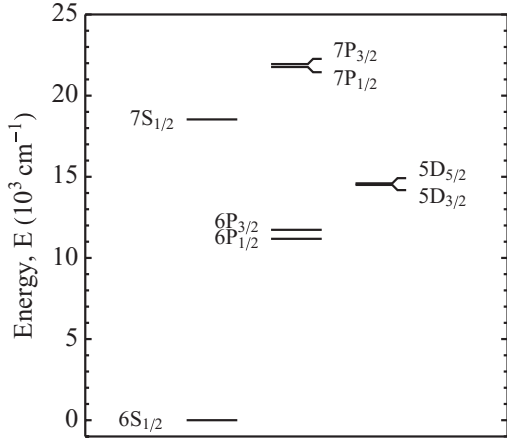[†]Correspondance address: glen.perram@afit.edu

FIG. 1. Some lower energy levels of cesium. The wavelengths and transition probabilities are listed in Table I.

where R is the optical pumping rate at $\lambda_{20} = 455.5$ nm, A_{10} and A_{20} are the spontaneous emission rates, and ξ_2 and ξ_1 are the radiation trapping factors discussed below. k_{20} and k_{10} are the quenching rates of the $J = 3/2$ and $J = 1/2$ levels, respectively, and k_{21} and k_{12} are the spin-orbit mixing rates in the forward and backward directions. The spin-orbit relaxation rates are related by detailed balance,

$$k_{12} = \frac{g_2}{g_1} e^{-\frac{\Delta E_{21}}{k_B T}} k_{21} = \rho k_{21}, \qquad (2)$$

where the degeneracies are $g_2 = 4$ and $g_1 = g_0 = 2$ for N_2, N_1, and N_0, respectively. k_B is the Boltzman's constant, $\Delta E_{21} =$

181 cm^{-1}, and at $T = 373$ K, $\rho = 0.9948$. The pump rate, R, is specified by pump laser intensity, $I_p(t)$:

$$R(t) = \frac{\sigma_{stim}}{h \nu_{20}} I_p(t) \left(\frac{g_2}{g_0} N_0 - N_2 \right), \qquad (3)$$

where h is the Planck's constant, ν_{20} is the frequency of the 2-0 pump transition, and σ_{stim} is the stimulated emission cross section of the 2-0 transition. The arbitrary collision partner, M, is either helium, methane, or ethane in the present work. First-order decay rates are defined as $\gamma_{20} = k_{20} [M]$, $\gamma_{10} = k_{10} [M]$, and $\gamma_{21} = k_{21} [M]$, where $[M]$ is the number density of the collision partner.

The coupled rate equations can be cast in matrix form [16]:

$$\begin{pmatrix} \dot{N_2} \\ \dot{N_1} \end{pmatrix} = \begin{pmatrix} -(\xi_2 A_{20} + \gamma_{20} + \gamma_{21}) & R + \rho \gamma_{21} \\ \gamma_{21} & -(\xi_1 A_{10} + \gamma_{10} + \rho \gamma_{21}) \end{pmatrix}$$
$$\times \begin{pmatrix} N_2 \\ N_1 \end{pmatrix}. \qquad (4)$$

When the duration of the pump pulse is short relative to the radiative and collisional time scales, the pump rate R can be converted to an initial condition for the number pumped to the $7\,^2P_{3/2}$ state: $N_2^0 = N_2(t = 0)$.

For instantaneous pumping, the rate equations in Eq. (4) have a time-dependent solution for the fluorescence intensity $I(t)$:

$$I(t) = C(e^{(-\lambda_- t)} - e^{(-\lambda_+ t)}), \qquad (5)$$

with eigenvalues

$$\lambda_\pm = -\frac{1}{2} [\xi_1 A_{10} + \xi_2 A_{20} + \gamma_{10} + \gamma_{20} + (1 + \rho)\gamma_{21}]$$
$$\pm \frac{1}{2} \sqrt{[(\xi_1 A_{10} + \gamma_{10}) - (\xi_2 A_{20} + \gamma_{20})] + 2\gamma_{21}[(\xi_1 A_{10} + \gamma_{10})(\rho - 1) + (\xi_2 A_{20} + \gamma_{20})(1 - \rho)] + (1 + \rho)^2 \gamma_{21}^2}. \qquad (6)$$

The coefficient describing the initial conditions, C, is pressure dependent and may be written as

$$C = \frac{\gamma_{21}}{\sqrt{[(\xi_1 A_{10} + \gamma_{10}) - (\xi_2 A_{20} + \gamma_{20})] + 2\gamma_{21} [\xi_1 A_{10} + \gamma_{21})(\rho - 1) + (\xi_2 A_{20} + \gamma_{20})(1 - \rho)] + (1 + \rho)^2 \gamma_{21}^2}}. \qquad (7)$$

For the present conditions, $\rho \approx 1$ and Eq. (6) can be reduced to

$$\lambda_\pm = -\frac{1}{2}(\xi_1 A_{10} + \xi_2 A_{20} + \gamma_{10} + \gamma_{20} + 2\gamma_{21}) \pm \frac{1}{2}\sqrt{[(\xi_1 A_{10} - \xi_2 A_{20}) + (\gamma_{10} - \gamma_{20})]^2 + 4\gamma_{21}^2}. \qquad (8)$$

Using the same argument, we can now simplify Eq. (7) to $C = \gamma_{21}/(\lambda_+ - \lambda_-)$ or

$$C = \frac{\gamma_{21}}{\sqrt{[(\xi_1 A_{10} - \xi_2 A_{20}) + (\gamma_{10} - \gamma_{20})]^2 + 4\gamma_{21}^2}}. \qquad (9)$$

The values of k_{21}, k_{10}, and k_{20} were calculated from Eqs. (8) and (9) using the eigenvalues of the fluorescence curves fit to

Eq. (5). Using a MATHEMATICA nonlinear least-squares fit, the difference of the eigenvalues in Eq. (8) provides k_{21} and also $k_{10} - k_{20}$. The sum of the eigenvalues in Eq. (8) returns $k_{10} + k_{20}$. These two equations were solved simultaneously to extract k_{10} and k_{20}. Equation (9) can be used as an independent check of the fit parameters in Eq. (8). The values of $\xi_1 A_{10}$ and $\xi_2 A_{20}$ were calculated in a similar way. The values for σ_{10}, σ_{20}, and σ_{21} were calculated assuming $k = \bar{v}\sigma$, with $\bar{v} = (8k_B T/\pi \mu)^{1/2}$, where $\bar{v}$ is the average speed of the collision

TABLE I. Transition wavelengths and probabilities for several dipole allowed transitions of cesium in Fig. 1.

Transition	Energy E (cm^{-1})	Wavelength λ (nm)(air)	Transition prob. A (10^6 s^{-1})	Line reference	Transition prob. reference
$5D_{3/2}$-$6P_{3/2}$	2766.95	3614.088	0.107	[29]	[30]
$5D_{5/2}$-$6P_{3/2}$	2864.53	3490.967	0.781	[29]	[31]
$7P_{1/2}$-$7S_{1/2}$	3229.81	3096.148	3.52	[29]	[32]
$5D_{3/2}$-$6P_{1/2}$	3320.98	3011.151	0.913	[29]	[30]
$7P_{3/2}$-$7S_{1/2}$	3410.86	2931.805	4.05	[29]	[32]
$7S_{1/2}$-$6P_{3/2}$	6803.22	1469.490	11.4	[29]	[32]
$7P_{1/2}$-$5D_{3/2}$	7266.09	1375.88	1.59	[29]	[32]
$7P_{3/2}$-$5D_{5/2}$	7349.55	1360.55	1.10	[29]	[32]
$7S_{1/2}$-$6P_{1/2}$	7357.26	1358.83	6.23	[29]	[32]
$7P_{3/2}$-$5D_{3/2}$	7447.14	1342.43	0.13	[29]	[32]
$6P_{1/2}$-$6S_{1/2}$	11178.268	894.347	28.63	[29]	[33]
$6P_{3/2}$-$6S_{1/2}$	11732.307	852.113	32.79	[29]	[33]
$7P_{1/2}$-$6S_{1/2}$	21765.348	459.317	0.793	[29]	[34]
$7P_{3/2}$-$6S_{1/2}$	21946.397	455.528	1.84	[29]	[34]

pair, k_B is the Boltzmann's constant, T is the cell temperature, and μ is the reduced mass.

Finally, the effects of the finite duration pump pulse can be considered by direct numerical simulation of the rate equations in Eq. (4). $I_p(t)$ is approximately a time-dependent Gaussian pulse with a FWHM of $\tau_p = 10$ ns, a peak intensity of $I_{\text{peak}} \approx 10^8$ W/cm^2, and a phase delay of t_0:

$$I_p(t) = I_{\text{peak}} e^{-4 \ln 2 \left(\frac{t - t_0}{\tau_p} \right)^2}. \tag{10}$$

B. Radiation trapping

For a given volume of atomic vapor, radiation emitted near a resonance line can be absorbed and emitted many times before escaping. The effects of radiation trapping at modest cell temperatures must be considered, especially at higher Cs densities where laser action may be expected. Detailed discussion of trapping in alkali-metal vapor and buffer gas mixtures may be found in Refs. [17–21]. The trapping coefficient ξ is defined as the number of times a photon is absorbed after traveling a distance r before being emitted [22]. For a cylindrical geometry ξ can be approximated for Doppler-broadened transitions,

$$\xi = \frac{1.60}{k_0 r \sqrt{\pi \ln(k_0 r)}}, \tag{11a}$$

with k_0 defined as

$$k_0 = \frac{\lambda^3}{8\pi} N_0 \frac{g_2}{g_0} \frac{A}{\sqrt{\pi} v_{\text{Cs}}}, \tag{11b}$$

and for pressure broadening,

$$\xi = \frac{1.115}{\sqrt{\pi k_p r}}, \tag{12a}$$

with k_p defined as

$$k_p = \frac{\lambda^2}{2\pi} N_0 \frac{g_2}{g_0} \frac{A}{\gamma_p}, \tag{12b}$$

where A is the Einstein A coefficient of the transition; r is the radial path length through the Cs vapor; γ_p is the collisional

broadening rate (s^{-1}), to include the effects of self and collision partner broadening [23]; v_{Cs} is the average velocity of Cs; and N_0 is the number density of Cs. For the Cs $7\,^2P_{3/2,1/2}$ states the collision rates are high and the present study is limited to low pressures of less than 2 Torr. Thus Doppler broadening dominates the trapping factors: ξ_1 and ξ_2 are independent of pressure. Only when pressure broadening is significantly larger can a pressure-dependent trapping factor complicate determination of the fine structure and quenching rates.
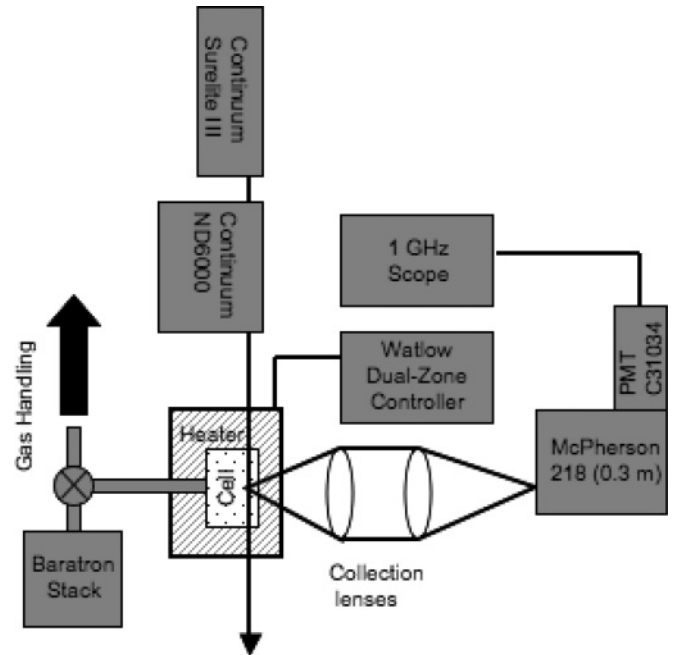

FIG. 2. Experiment layout. A heated glass cell contains about 1 g of pure cesium. A 10-ns pulsed dye laser at 455.5 nm pumps the Cs $7\,^2P_{3/2}$-$6S_{1/2}$ transition and side fluorescence is monitored via an RCA 31034 PMT attached to a 0.3-m $f/5$ monochromator and recorded using a 1-GHz oscilloscope.
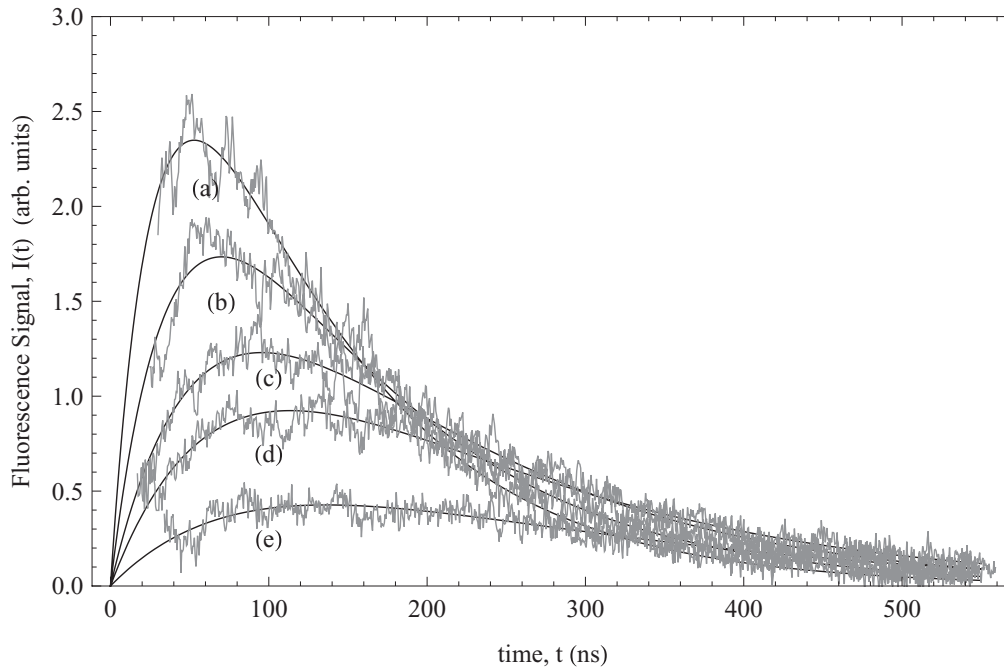
FIG. 3. Helium fluorescence decay curves of the cesium $7P_{1/2}$-$6S_{1/2}$ transition (459.3 nm) at 50 °C using a 10-ns pulsed dye laser at 455.5 nm. The solid curves are the least-squares fit of Eq. (5). The buffer gas pressures in Torr are (a) 2.0, (b) 1.2, (c) 0.6, (d) 0.4, and (e) 0.2.

III. EXPERIMENT

The pulsed, laser-induced fluorescence apparatus is shown schematically in Fig. 2. A pulsed dye laser (Continuum ND6000), with up to 25 mJ in a 10-ns pulse at 10 Hz was tuned to the cesium $7\,^2P_{3/2}$-$6S_{1/2}$ (λ_{20}, 455 nm) transition. The pump bandwidth is about 2.1 GHz, large compared to the Doppler-broadened absorption profile. The fluorescence of the cesium $7\,^2P_{1/2}$-$6S_{1/2}$ transition (λ_{10}, 459 nm) was collected with a pair of lenses ($f1 = 90$ mm, $f2 = 250$ mm) and the image was focused on the entrance slit of a McPherson 218 (0.3 m) monochromator with a resolution of 0.5 nm. The fluorescence was detected with an uncooled RCA 31034 photomultiplier tube and analyzed on a 1-GHz oscilloscope. The cesium was contained in a Pyrex cylinder (25.4-mm radius) enclosed in an aluminum heater block with an observation port perpendicular to the pump beam. The cell temperature was controlled
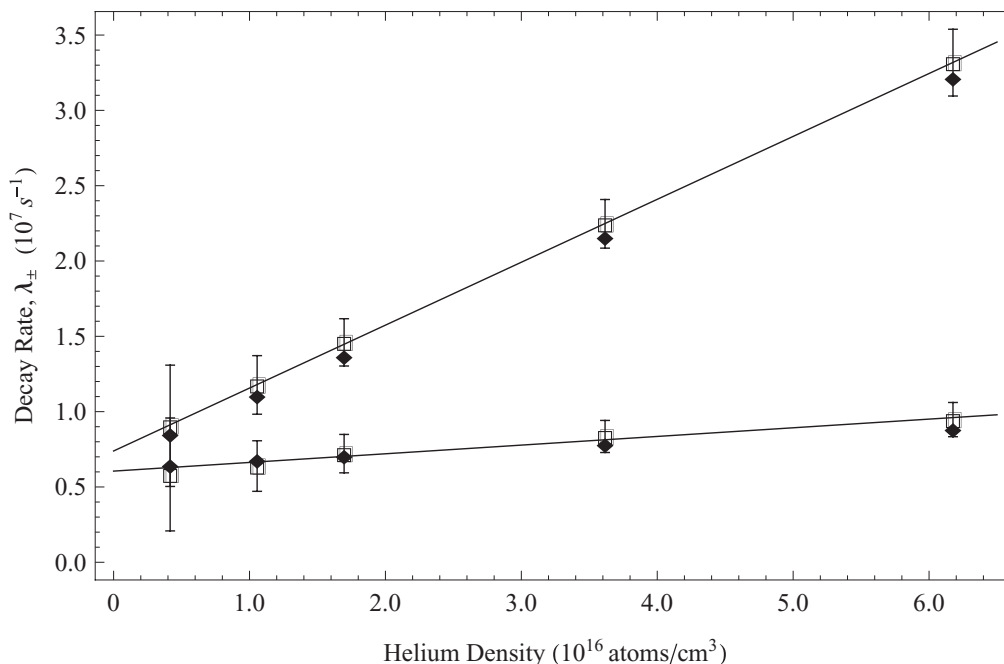

FIG. 4. Stern-Volmer plot of experimentally derived rates (□) and calculated rates based on Eq. (8) (◆) for helium at 50 °C. The solid line is a least-squares linear fit to the experimentally derived rates.
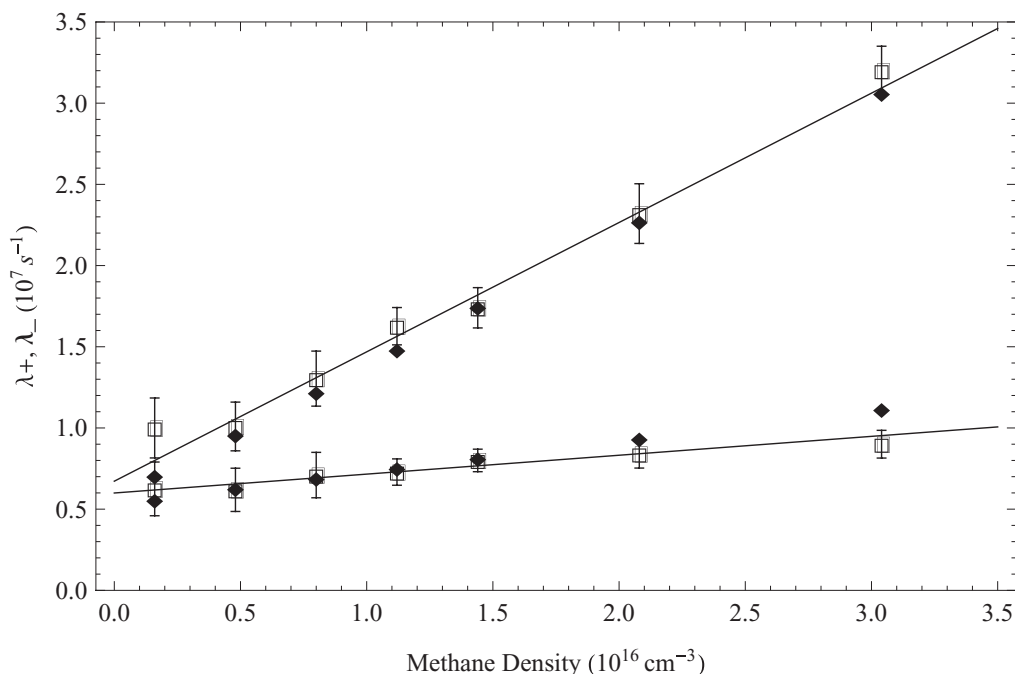
FIG. 5. Stern-Volmer plot of experimentally derived rates (□) and calculated rates based on Eq. (8) (◆) for methane at 110 °C. The solid line is a least-squares linear fit to the experimentally derived rates.

($\pm 1\,°C$) using a dual-zone heater system (Watlow) with independent control of both the cell and the cold finger. For these experiments the cell temperature was maintained about $5\,°C$ above the cold finger to prevent condensation on the cell windows. At $110\,°C$ the concentration of Cs is about 3.4×10^{16} atoms/cm^3. For C_2H_6 we found that a temperature of $120\,°C$ was required to create an acceptable signal-to-noise ratio. At this temperature the concentration of Cs is about double that of

$110\,°C$. The cells were baked for several hours at $250\,°C$ under vacuum (10^{-6} Torr) before breaking the ampoule containing the cesium metal. Research grade He, CH_4, and C_2H_6 gas pressure was measured with Baratron capacitance manometers (Model No. 690A) with 0.001–1000 Torr ranges. For each pressure the scattered pump laser intensity was subtracted from the observed decay profiles by tuning off the resonance and recording the part of the signal not attributed to fluorescence.
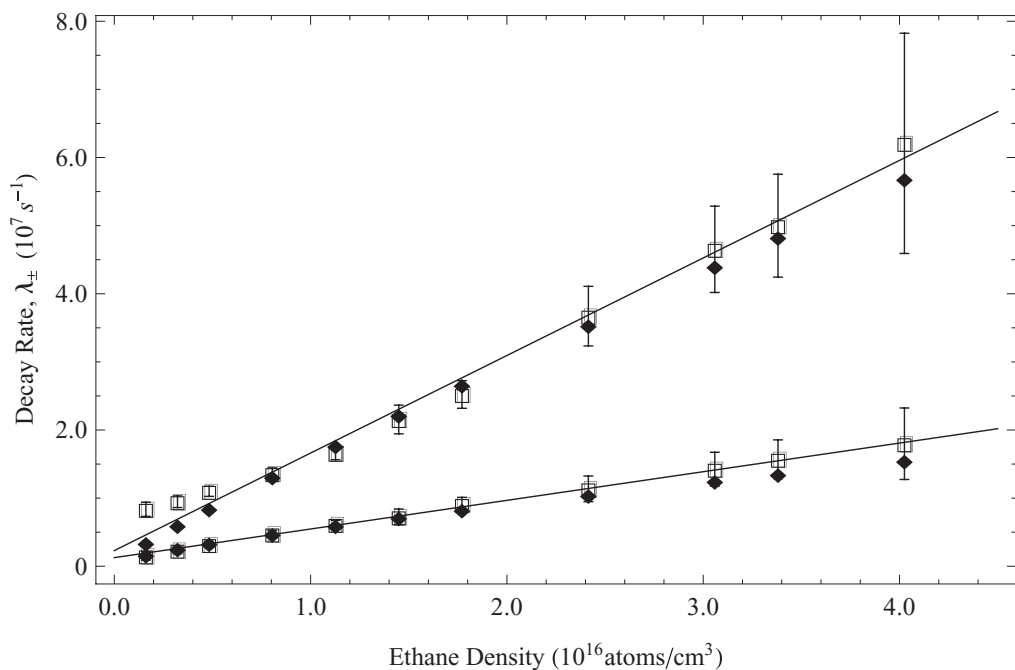

FIG. 6. Stern-Volmer plot of experimentally derived rates (□) and calculated rates based on Eq. (8) (◆) for ethane at 120 °C. The solid line is a least-squares linear fit to the experimentally derived rates.
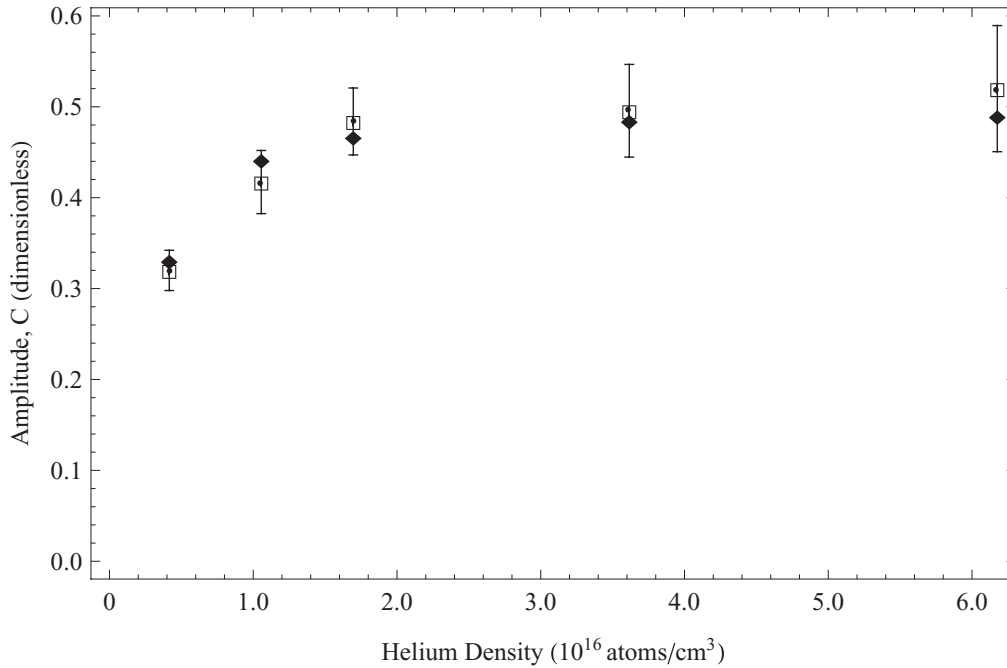
FIG. 7. Plot of the amplitude C from the fit of Eq. (5) ($\square$) and predicted by Eq. (9) ($\blacklozenge$) for helium.

IV. RESULTS

The fluorescence decay curves for emission from $7\,^2P_{1/2}$ for various He buffer gas pressures are provided in Fig. 3. As buffer gas increases, the rate for spin-orbit relaxation increases, the peak fluorescence intensity increases, and decay rates increase. A significant population is transferred even at low pressure, indicating near gas kinetic rates. Scattered laser light obscures the decay curves for $t < 20$ ns. For each pressure, the decay curves were fit to the double exponential function of Eq. (5) generating the two eigenvalues λ_+ and λ_- and the amplitude coefficient C. The fits are compared with the data in Fig. 3.

The pressure dependence of the fit eigenvalues are displayed as Stern-Volmer plots for He, CH$_4$, and C$_2$H$_6$ collision partners in Figs. 4–6. The intercepts on the Stern-Volmer plot for helium (Fig. 4) are nearly equal for the two eigenvalues, agree to within 2–5% of the known radiative rates of $A_{20} = 7.5 \times 10^6$ s^{-1} and $A_{10} = 6.3 \times 10^6$ s^{-1} [9]. Under the $T = 50\,°$C cell conditions for the helium data, radiation trapping is minimal. However, for the higher temperatures (and thus Cs concentrations) required of methane and ethane, the intercepts diverge and the corresponding effective rates suggest trapping factors of $\xi = 0.81$–0.92 ± 0.16 for $T = 110\,°$C (CH$_4$) and $\xi = 0.20$–0.31 ± 0.4 for $T = 120\,°$C (C$_2$H$_6$). The error bounds in the Stern-Volmer plots represent a confidence interval of 99%. The uncertainty in the pressure is small, $\approx 1\%$. The drift in absolute pressures is less than 15 mTorr.

The trapping factors ξ are independent of He and CH$_4$ pressure, suggesting that Doppler broadening dominates the transition at the low buffer gas pressures. This seems probable since the Doppler broadening of Cs at those temperatures is about 800 MHz, whereas the Cs-He broadening is only about 10 MHz at the highest pressure. The value of ξ for ethane is smaller and weakly dependent on ethane pressure. This suggests that at the Lorentzian wing of the ethane broadened transition contributes to the radiation trapping. This "persistence" of the Lorentzian wing in radiation trapping has been mentioned before by Huennekens in mixtures of sodium and noble gases [19].

TABLE II. Cesium $7\,^2P$ effective radiative rates, spin-orbit and quenching cross sections assuming unequal quenching cross sections of the fine-structure states, calculated from Eqs. (8) and (9) (top) and values used in the simulations of Fig. 10 (bottom). Cell temperatures are given in parentheses.

Collision partner	Spin-orbit cross section (Å^2)	Quenching cross section ($J = 3/2$) (Å^2)	Quenching cross section ($J = 1/2$) (Å^2)
Helium	14 ± 2 (323 K)	5 ± 1	≈1
Methane	42 ± 3 (383 K)	30 ± 2	20 ± 2
Ethane	80 ± 5 (393 K)	80 ± 6	10 ± 3
Helium	14 ± 3 (323 K)	4 ± 3	≈1
Methane	35 ± 6 (383 K)	45 ± 8	25 ± 2
Ethane	73 ± 10 (393 K)	59 ± 6	31 ± 3

TABLE III. Cesium $7\,^2P$ spin-orbit and quenching cross sections from previous works. Cell temperatures are given in parentheses.

Collision partner	Spin-orbit, σ_{21}, cross section (Å^2)	Quenching, $\sigma_{10} = \sigma_{20}$, cross section (Å^2)	Reference
Helium	12.8 ± 2.6 (320 K)	Not reported	[9]
Helium	11 ± 2 (448 K)	Not reported	[10]
Helium	14.9 ± 4.5 (320 K)	Not reported	[11]
Helium	15.2 ± 4.6 (320 K)	Not reported	[11]
Methane	40	60	[12]

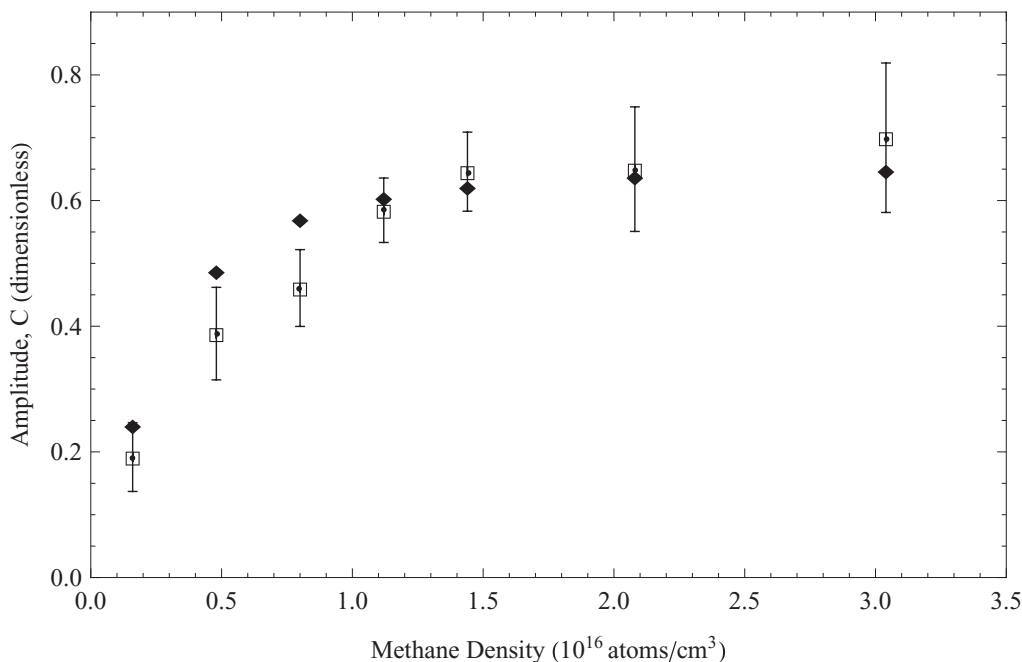FIG. 8. Plot of the amplitude C from the fit of Eq. (5) ($\square$) and predicted by Eq. (9) ($\blacklozenge$) for methane.

The amplitudes for the decay curves C obtained from the fit to Eq. (9) as a function of buffer gas concentration are shown in Figs. 7–9. The error bounds for these plots represent a confidence interval of 90%. The amplitude would be independent of pressure if the radiative and quenching rates were equal for the two spin-orbit split states. However, the significant curvature in Figs. 7–9 is consistent with the prediction of Eq. (9), establishing the variance in quenching rates reported in Table II. The eigenvalues predicted from Eq. (6) are wholly consistent with the observations, as illustrated in

Figs. 4 and 6. Indeed, the three pressure-dependent quantities, $\lambda_\pm$ and C, uniquely define the three cross sections, σ_{20}, σ_{10}, and σ_{21}.

Finally, the full numerical integration of the rate equations (4) with the time-dependent pumping of Eq. (10) is compared to the observed decay profiles for the ethane case in Fig. 10. A single set of cross sections, as summarized in Table II, is sufficient to represent the full set of observed decay profiles. These results represent the best estimate for the spin-orbit relaxation and quenching cross sections reported
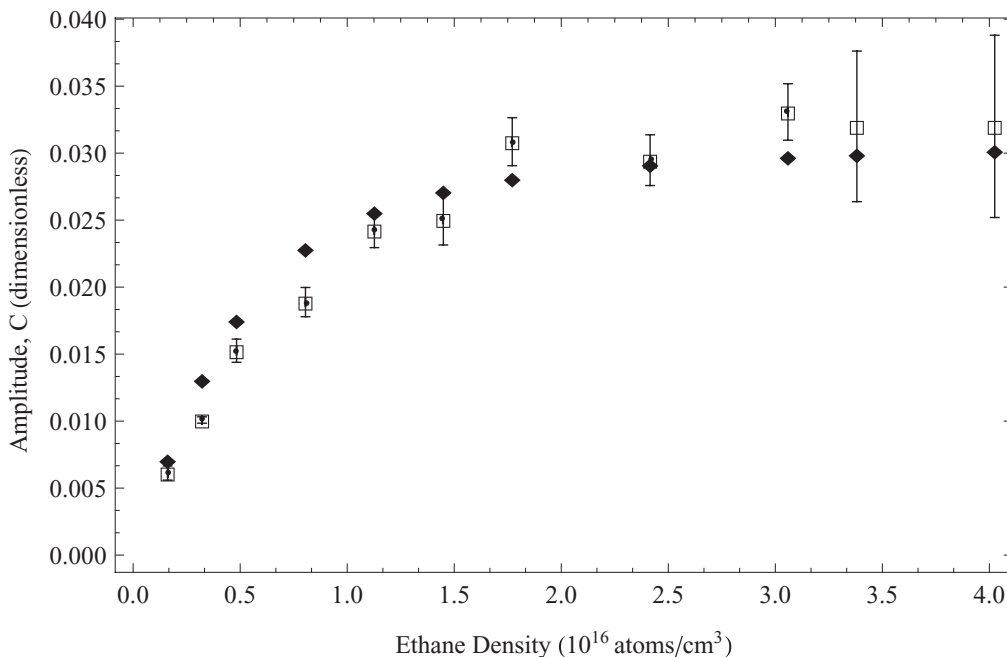

FIG. 9. Plot of the amplitude C from the fit of Eq. (5) ($\square$) and predicted by Eq. (9) ($\blacklozenge$) for ethane.
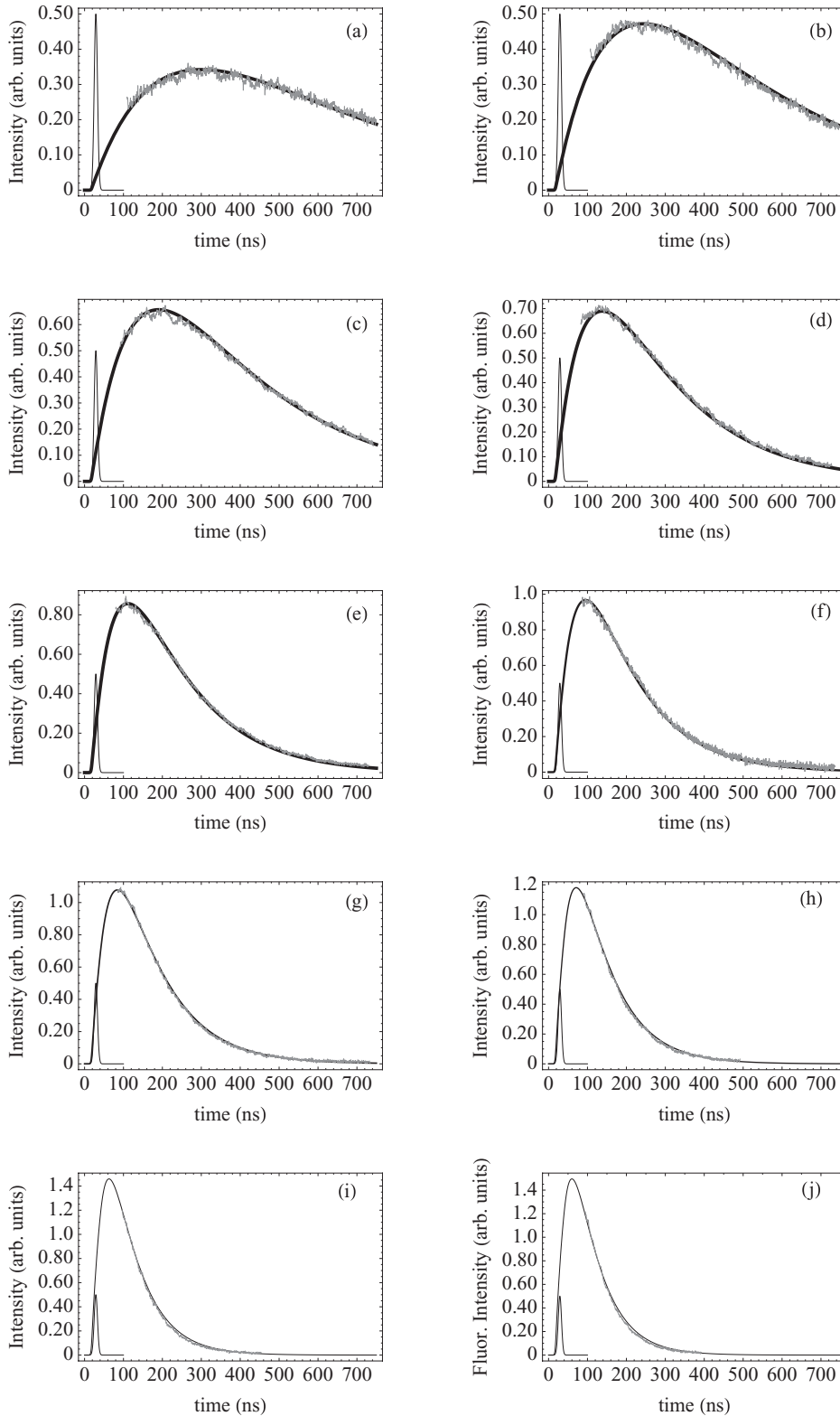
FIG. 10. Simulated side fluorescence plots (solid) with data for ethane at $T = 120\,^{\circ}\mathrm{C}$. The buffer gas pressures in Torr are (a) 0.1, (b) 0.15, (c) 0.2, (d) 0.3, (e) 0.4, (f) 0.5, (g) 0.6, (h) 0.8, (i) 1.0, and (j) 1.1.

in this work. The simultaneous representation of all the decay profiles by a single set of rate coefficients illustrates the self-consistency of the observations and analysis. The uncertainties in the spin-orbit relaxation rates are somewhat larger when all the data are simultaneously analyzed with the numerical simulations. The spin-orbit rates agree within the error bounds. The consistency of the quenching rates is poorer,

suggesting systematic error bounds for the quenching rates of 35%.

V. DISCUSSION

While the fine-structure mixing and quenching of the first excited $^2P_{3/2,1/2}$ states in the alkali-metal atoms is well studied [9–15,24], the kinetic database for the higher-lying

states is rather limited [9,10,15]. The rates for Cs $7\,^2P_{3/2,1/2}$ with helium and methane collision partners have previously been determined and are summarized in Table III. The current measurements of the spin-orbit relaxation rates for He and CH_4 agree favorably with the prior results. Indeed, there is no discrepancy considering the 20% error bands. We are not aware of any prior results of ethane.

The fine-structure mixing rates for the first excited Cs $6\,^2P_{3/2,1/2}$ states with rare gas partners are sufficiently rapid to sustain near-infrared lasing only for the K and Rb diode pumped alkali-metal laser systems [1,25]. For the heavier alkali-metal atoms the fine-structure splitting increases and the mixing rates decrease. This trend has been qualitatively explained in terms of collision adiabaticity [13]. When the duration of the collision, τ_c, is long relative to the period of oscillation, $\tau_\nu = 1/\nu_{21} = h/\Delta E_{21}$, the interaction is adiabatic and the mixing probability is low. For light collision partners where the relative speed is high, the collision time decreases, the interaction is more impulsive, or sudden, and the mixing rate increases. We define adiabaticity, α, as the ratio of the oscillator period and collision duration:

$$\alpha = \frac{\tau_\nu}{\tau_c} = \frac{\bar{v}}{\nu_{21}L}, \tag{13}$$

where the collision time is determined from the characteristic interaction length L and the relative speed $\bar{v}$. The current results for helium are compared with prior studies of the Cs $n = 6, 7,$ and $8\,^2P_{3/2,1/2}$ and $5\,^2D_{5/2,3/2}$ levels in Fig. 11. Cross sections are reported as a probability per collision by normalizing relative to the gas kinetic value, $\sigma_g = \pi\,(r_{Cs} + r_{He})^2 = 9.9 \times 10^{-15}$ cm^2. For a fixed interaction length, $L = 0.2$ nm, and given collision pair, $\bar{v} = 1.5$–1.8×10^5 cm/s at $T = 420$–601 K, the adiabaticity depends primarily on the fine-structure splitting. The results are nicely summarized by this single parameter. The cross sections increase linearly with the inverse of the adiabaticity, until a near unit probability per collision is reached. The $8\,^2P$ term has the smallest spitting, $\Delta E_{21}/k_BT = 0.29$, yielding a near gas kinetic rate.
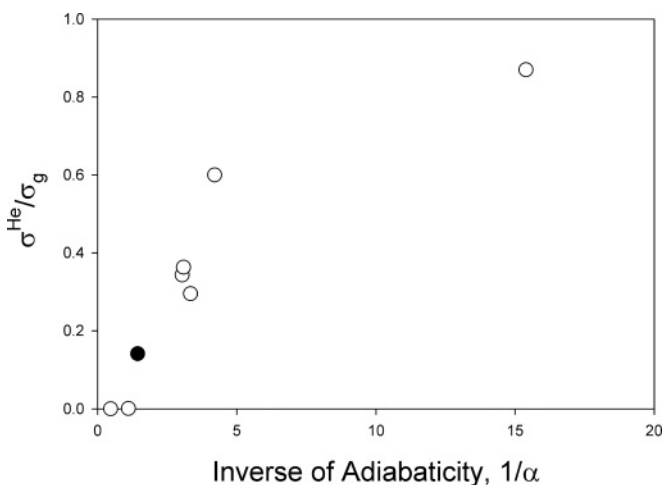

FIG. 11. Scaling of the fine-structure mixing cross sections, σ_{21}, with adiabaticity for He collisions with the lowest ^2P states of Cs, Rb, K, and Na and the higher excited $n = 7, 8\,^2P$ and $n = 5\,^2D$ states of Cs: (○) prior data [14–16] and (●) present result for Cs $7\,^2P$.
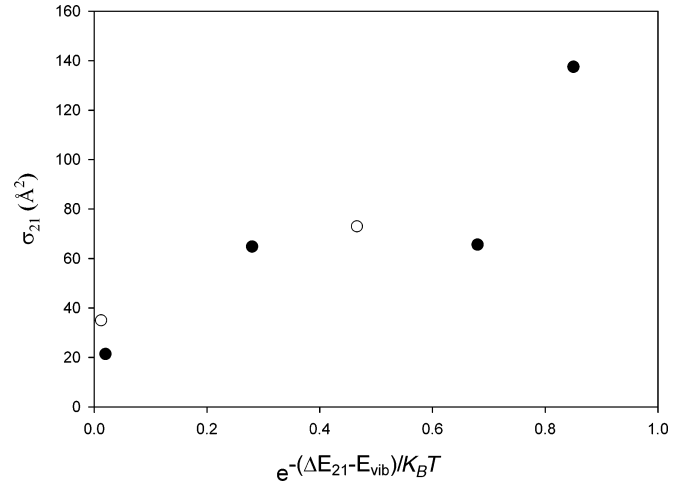

FIG. 12. Scaling of fine-structure mixing cross sections with vibrational energy defect for (●) Cs $6\,^2P_{3/2,1/2}$ [14] and (○) Cs $7\,^2P$ (present results). Buffer gases include CH_4, C_2H_6, and C_2F_6.

Mixing induced by the molecular collision partners is generally faster than that induced by the rare gases. Recent studies of mixing in Rb $5\,^2P_{3/2,1/2}$ and Cs $6\,^2P_{3/2,1/2}$ by molecular collision partners attribute the efficient collisional mixing to rovibrational excitation [14,15]. The splitting in Cs $7\,^2P_{3/2,1/2}$ of 181 cm^{-1} is more nearly resonant with the 289 cm^{-1} vibrational mode of ethane than the lowest, 1367 cm^{-1}, mode of methane, leading to an enhancement in the mixing rate. The scaling with energy defect for the present study of Cs $7\,^2P$ is consistent with the recent results for Cs $6\,^2P$, as shown in Fig. 12.

Several prior studies of inelastic collisions between alkali metals and rare gases or small molecules report quenching rates that depend on fine-structure splitting. Generally, the $J = 3/2$ level exhibits a rate that is faster than that of the $J = 1/2$ component by a factor of up to 4.5 [26]. However, the $J = 1/2$ state is more rapidly quenched in mixtures of Cs($6\,^2P_{1/2}$) + (H_2, HD, or CH_4) [27], and equally quenched in mixtures of K($4\,^2P_{1/2}$) + C_2H_4 [28]. The current results of Table II indicate ratios of σ_{20}/σ_{10} of 4.1, 1.8, and 1.9 for helium, methane, and ethane, respectively. For molecular collision partners, spin-orbit mixing rates in Rb and Cs have been attributed to electronic to rovibrational energy transfer [14]. Resonances in the molecular energy transfer might explain the strong dependence on spin-orbit splitting.

The efficiency of the diode-pumped alkali laser depends in part on rapid fine-structure mixing without significant quenching. Quenching may compete with the pump rate and effectively increase the pump intensity required to reach threshold. Helium, methane, and ethane collision partners meet these criteria for the first $^2P_{3/2,1/2}$ states associated with the near-infrared lasers. For the blue analog laser, intermultiplet energy transfer is possible and quenching rates may be enhanced.

The present results indicate quenching for Cs $7\,^2P_{3/2,1/2}$ by helium is about 35% of the fine-structure mixing. Our full numerical analysis agrees that the quenching of Cs $7\,^2P_{3/2}$ by methane is about 28% greater than the fine-structure mixing. The ethane collision partner is somewhat more favorable for

lasing, with a mixing rate more than twice that for methane. The ethane quenching rate remains large and significantly impacts laser performance. Indeed, our recent demonstration of a blue laser directly pumped on the Cs $6\,^2S_{1/2}$-$7\,^2P_{3/2}$ transition requires ethane as the collision partner [8]. Clearly, the performance of the blue analog laser is degraded by the rapid quenching rates and the search for alternative buffer gas partners is warranted.

VI. CONCLUSION

Collision-induced mixing in Cs $7\,^2P_{3/2,1/2}$ is rapid, due to the small energy splitting. The scaling of helium-induced mixing rates among the various excited Cs states is well described by a single parameter, the adiabaticity. The mixing rates by molecular collision partners are somewhat larger and appear to be enhanced by vibrational energy transfer. In contrast to the lowest, Cs $6\,^2P_{3/2,1/2}$, levels, the higher excited states are rapidly quenched. Intermultiplet energy transfer likely enhances the quenching rates. Quenching of the blue laser upper level, $7\,^2P_{1/2}$, by ethane is about 42% of the fine-structure mixing rate. While a blue laser with direct optical pumping of $7\,^2P_{3/2}$ has been demonstrated, the rapid quenching imposes an increased pump rate to reach threshold and a higher heat load.

[1] W. Krupke, R. Beach, V. Kanz, and S. Payne, Opt. Lett. **28**, 2336 (2003).

[2] B. V. Zhdanov, T. Ehrenreich, and R. J. Knize, Opt. Commun. **260**, 696 (2006).

[3] T. Perschbacher, D. A. Hostutler, and T. Shay, in *Proc. SPIE* **6346**, 634607 (2006).

[4] J. Zweiback, A. Komashko, and W. Krupke, in *Proc. SPIE* **7581**, 75810G (2010).

[5] C. V. Sulham, G. P. Perram, M. P. Wilkinson, and D. A. Hostutler, Opt. Commun. **283**, 4328 (2010).

[6] W. Miller, C. Sulham, J. Holtgrave, and G. Perram, Appl. Phys. B **103**, 819 (2011).

[7] R. H. Page and R. J. Beach, *Diode-Pumped Alkali Atom Lasers*, Technical Report, Lawrence Livermoore National Laboratory, https://e-reports-ext.llnl.gov/pdf/316721.pdf, 2004.

[8] K. C. Brown and G. P. Perram, in *Proc. SPIE* **7915**, 791507 (2011).

[9] P. Munster and J. Marek, J. Phys. B **14**, 1009 (1981).

[10] J. Cuvellier, P. R. Fournier, F. Gounand, J. Pascale, and J. Berlande, Phys. Rev. A **11**, 846 (1975).

[11] I. Siara, H. Kwong, and L. Krause, Can. J. Phys. **52**, 945 (1974).

[12] I. Siara, R. U. Dubois, and L. Krause, Can. J. Phys. **60**, 239 (1982).

[13] A. Gallagher, Phys. Rev. **172**, 88 (1968).

[14] G. A. Pitz, C. D. Fox, and G. P. Perram, Phys. Rev. A **84**, 032708 (2011).

[15] L. Krause, Appl. Opt. **5**, 1375 (1966).

[16] A. Sasso, W. Demtroder, T. Colbert, C. Wang, E. Ehrlacher, and J. Huennekens, Phys. Rev. A **45**, 1670 (1992).

[17] T. Colbert and J. Huennekens, Phys. Rev. A **41**, 6145 (1990).

[18] A. Molisch, B. Oehry, W. Schupita, and G. Magerl, J. Quantum Spectrosc. Radiat. Transfer **49**, 361 (1993).

[19] J. Huennekens, H. J. Park, T. Colbert, and S. C. McClain, Phys. Rev. A **35**, 2892 (1987).

[20] M. Rosenberry, J. Reyes, D. Tupa, and T. Gay, Phys. Rev. A **75**, 023401 (2007).

[21] N. D. Zameroski, W. Rudolph, G. D. Hager, and D. A. Hostutler, J. Phys. B **42**, 245401 (2009).

[22] T. Holstein, Phys. Rev. **72**, 1212 (1947).

[23] J. Huennekens and A. Gallagher, Phys. Rev. A **28**, 238 (1983).

[24] M. D. Rotondaro and G. P. Perram, Phys. Rev. A **58**, 2023 (1998).

[25] J. Zwieback, G. D. Hager, and W. F. Krupke, Opt. Commun. **282**, 1871 (2009).

[26] D. McGillis and L. Krause, Phys. Rev. **153**, 44 (1967).

[27] I. Siara and L. Krause, Can. J. Phys. **51**, 257 (1973).

[28] B. Earl and R. R. Herm, J. Chem. Phys. **60**, 4568 (1974).

[29] J. E. Sansonetti and W. C. Martin, J. Phys. Chem. Ref. Data **34**, 1559 (2005).

[30] M. S. Safronova and C. W. Clark, Phys. Rev. A **69**, 040501 (2004).

[31] D. DiBerardino, C. E. Tanner, and A. Sieradzan, Phys. Rev. A **57**, 4204 (1998).

[32] O. Heavens, J. Opt. Soc. Am. **51**, 1058 (1961).

[33] R. J. Rafac, C. E. Tanner, A. E. Livingston, K. W. Kukla, H. G. Berry, and C. A. Kurtz, Phys. Rev. A **50**, R1976 (1994).

[34] A. A. Vasilyev, I. M. Savukov, M. S. Safronova, and H. G. Berry, Phys. Rev. A **66**, 020101 (2002).